

To be submitted to ApJ

The Dwarf Starburst Host Galaxy of a Type Ia SN at $z = 1.55$ from CANDELS¹

Teddy F. Frederiksen², Jens Hjorth², Justyn R. Maund^{2,3,4}, Steven A. Rodney⁵, Adam G. Riess^{5,6}, Tomas Dahlen⁶, Bahram Mobasher⁷

teddy@dark-cosmology.dk

ABSTRACT

We present VLT/X-shooter observations of a high redshift, type Ia supernova host galaxy, discovered with *HST*/WFC3 as part of the CANDELS Supernova project. The galaxy exhibits strong emission lines of Ly α , [O II], H β , [O III], and H α at $z = 1.54992^{+0.00008}_{-0.00004}$. From the emission-line fluxes and SED fitting of broad-band photometry we rule out AGN activity and characterize the host galaxy as a young, low mass, metal poor, starburst galaxy with low intrinsic extinction and high Ly α escape fraction. The host galaxy stands out in terms of the star formation, stellar mass, and metallicity compared to its lower redshift counterparts, mainly because of its high specific star-formation rate. If valid for a larger sample of high-redshift SN Ia host galaxies, such changes in the host galaxy properties with redshift are of interest because of the potential impact on the use of SN Ia as standard candles in cosmology.

Subject headings: galaxies: abundances — galaxies: distances and redshift — galaxies: starburst

² Dark Cosmology Centre, Niels Bohr Institute, University of Copenhagen, Juliane Maries Vej 30, 2100 Copenhagen, Denmark

³ Astrophysics Research Centre, School of Mathematics and Physics, Queen's University Belfast, University Road, Belfast BT7 1NN, Northern Ireland, UK

⁴Royal Society Research Fellow

⁵ Department of Physics and Astronomy, The Johns Hopkins University, Baltimore, MD 2121

⁶ Space Telescope Science Institute, Baltimore, MD 21218

⁷ Department of Physics and Astronomy, University of California, Riverside, CA 9252

¹Based on observations made with ESO telescopes at the La Silla Paranal Observatory under program ID 086.A-0660

1. INTRODUCTION

Type Ia Supernovae (SNe Ia) are cornerstones of modern cosmology because of their properties as luminous standard candles. The development of these important cosmological tools began in the late 1930’s when Zwicky (1938) and Wilson (1939) first suggested that SNe could be used as distance indicators. Theoretical developments in the 1960’s suggested that SNe of type Ia form a homogenous class of objects with a measured peak magnitude of $M_B \approx -19.3 + 5 \log h_{70}$ (for a modern review, see Hillebrandt & Niemeyer 2000; Kirshner 2010). To first approximation, the light curves of SN Ia form a one-parameter family of models, driven by the decay of radioactive $^{56}\text{Ni} \rightarrow ^{56}\text{Co} \rightarrow ^{56}\text{Fe}$. The amount of radioactive nickel produced in the initial explosion therefore dictates the shape of the light curve. Later observational work showed that the scatter in the peak magnitude is correlated with other SN properties, such as light curve shape and color (Phillips 1993; Riess et al. 1996; Phillips et al. 1999).

SN cosmology achieved its modern prominence at the close of the millennium with the discovery of the accelerating expansion of the universe, based on just a few dozen objects (Perlmutter et al. 1999; Riess et al. 1998). Nearly 15 years later, modern SNIa samples can now include over 500 well-studied SNe with a dispersion in peak magnitudes of ~ 0.16 magnitudes (e.g., Conley et al. 2011; Suzuki et al. 2012). At this precision, a larger sample size alone will not improve cosmological constraints, so the limiting factor is our understanding of systematic effects.

Among the major concerns for systematic biases is the fact that we still do not have a complete or conclusive description of the SN Ia progenitor systems. Indeed, there may be several viable progenitor pathways (known as single and double degenerate models, see Wang & Han 2012, for a review), possibly leading to slightly different explosion characteristics. One might expect different progenitor pathways to be correlated with differences in SN environment, and such correlations with host galaxy properties have recently been observed (Hamuy et al. 2000; Kelly et al. 2010; Lampeitl et al. 2010; Sullivan et al. 2010). Correcting for this effect with measurement of the host galaxy stellar mass brings the dispersion in absolute peak magnitude down to ~ 0.1 magnitudes (Conley et al. 2011; March et al. 2011). This signature of environmental effects calls for further characterization of the host galaxies when SNe are used for cosmography. Riess & Livio (2006) discuss how a change in the progenitor population (like progenitor metallicity and age) at $1.5 < z < 3.0$ could affect the inferred distance in a way inconsistent with dark energy models. The redshift window $1.5 < z < 3.0$ is therefore favorable for disentangling systematic effects arising from environment.

The Cosmic Assembly Near-IR Deep Extragalactic Legacy Survey (CANDELS) survey

(Grogin et al. 2011) is a Hubble Space Telescope (HST) multi-cycle treasury (MCT) program designed to detect high redshift SNe. The CANDELS collaboration is surveying five well-observed fields (GOODS-N, GOODS-S, COSMOS, EGS and UDF). With this observation strategy CANDELS will find SNe Ia out to redshifts of ~ 2 (see Rodney et al. 2012). The first SN detected in the CANDELS survey was discovered 2010 October 14 in the GOODS-S field and was nicknamed SN Primo. Rodney et al. (2012) present the light curve and grism spectrum of this SN, concluding that SN Primo was of type Ia.

The aim of this paper is to characterize the host galaxy of SN Primo. We derive its spectral properties from spectroscopic emission-line fluxes and fit the spectral energy distribution (SED) based on broad-band photometry to constrain its stellar population. We then compare the properties of the host galaxy of SN Primo with its counterparts at lower redshifts and discuss sources of bias when using high redshift SNe as standard candles.

The paper is structured as follows: In Section 2 we present the spectra and photometric data. In Section 3 we perform the SED fitting using broad-band photometry to get stellar mass and stellar age and we derive the emission-line fluxes and calculate spectral properties like metallicity and the Lyman- α escape fraction. Finally, a discussion and conclusions are given in Section 4. We assume a flat Λ CDM cosmology, with $H_0 = 70.2 \text{ km s}^{-1} \text{ Mpc}^{-1}$ and $\Omega_m = 0.274$ (Komatsu et al. 2011). All magnitudes given in this paper are AB magnitudes.

2. DATA

2.1. Spectroscopic Data

The host of SN Primo is located in the GOODS-S field at R.A. = $03^{\text{h}}32^{\text{m}}22^{\text{s}}.64$ and decl. = $-27^{\circ}46'38''.66$ (J2000). The spectroscopic observations were performed on 2010 October 16, using the X-shooter instrument on the ESO Very Large Telescope (VLT) at Paranal Observatory, Chile (D’Odorico et al. 2006; Vernet et al. 2011). X-shooter is a cross-dispersed Echelle spectrograph with a large wavelength coverage from the UV to the Near IR (300 – 2500 nm). This is achieved by splitting the light beam into three wavelength regions and sending them into three different spectrographs (so-called arms) designated UVB (for UV and Blue, $\sim 300 - 550 \text{ nm}$), VIS (for Visual, $\sim 550 - 1000 \text{ nm}$), and NIR (for Near IR, $\sim 1000 - 2500 \text{ nm}$). For the observation we used an ABAB on-source nodding template with an exposure time of 1.3 hr ($4 \times 1200 \text{ sec}$). A $0''.9$ slit² with a PA of -35° E of N was placed to cover both the host and the SN (see Figure 1). The observations were conducted under

²A $1''.0$ slit in the UVB arm.

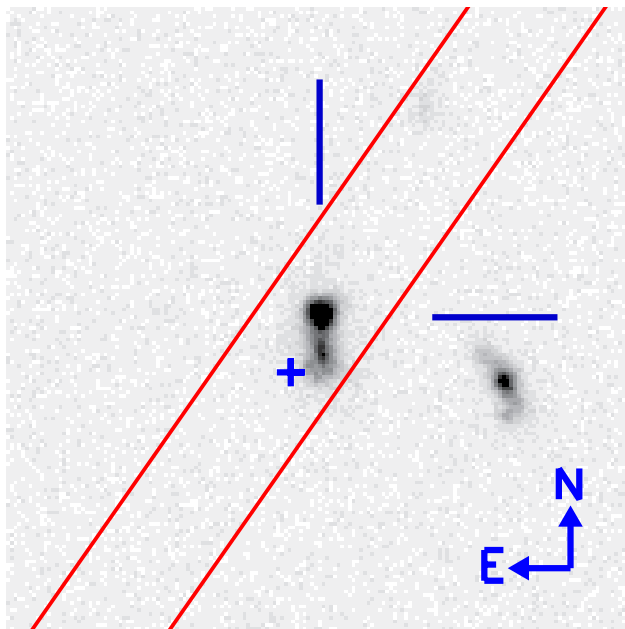


Fig. 1.— Pre-explosion *HST* F775W (i-band, rest frame u-band) image with the X-shooter slit configuration overlaid (red). The peak luminosity of the host galaxy is marked by ticks (blue). The size of the tick marks is $1''$, corresponding to 8.6 kpc at the redshift of SN Primo. The faint part to the south is also part of the galaxy (see Rodney et al. 2012). The location of the SN is marked by a plus (blue).

photometric conditions, with a median seeing³ of $0''.54$.

The X-shooter spectra were reduced using the official X-shooter pipeline⁴ v1.3.7. We achieved resolving powers of $R = 5400 \pm 360$ (UVB), $R = 7450 \pm 300$ (VIS), and $R = 5800 \pm 180$ (NIR). The extraction of the object spectra was conducted with our own IDL script, and flux calibration was done using the *HST* flux standard star, GD71⁵.

Even though the SN was still bright it was not detected in the spectrum (see Figure 3); only narrow emission lines from the host galaxy were visible with no trace of any continuum emission from either host or SN.

2.2. Flux Calibration Quality

We checked the quality of the flux calibration using a telluric standard star (HIP 018926) taken prior to the science exposure. The telluric standard star was of stellar type B3V, and has a high signal-to-noise ratio ($\sim 50 - 300$ per wavelength bin, $0.04 - 0.1$ nm per bin). The telluric standard star was reduced, extracted and flux calibrated in the same way as the science exposure. The flux calibrated spectrum agrees with the published photometric data points. A model spectrum of a B3V star was scaled to the photometric data and compared to the flux calibrated spectrum. The agreement between the model and the spectrum was within 5–10%, consistent with the expected quality of the flux calibration for X-shooter⁶ at the wavelengths of the lines detected in the science exposures (except at the location of Ly α). At an observed wavelength of 310 nm Ly α is close to the spectral lower limit of the UVB arm (300 nm). The discrepancy between the model and the telluric spectrum is $\sim 40\%$, i.e., the conversion factor between counts and cgs units is too large and will overestimate the flux of Ly α . We are therefore cautious when drawing conclusions based on the flux of the Ly α line.

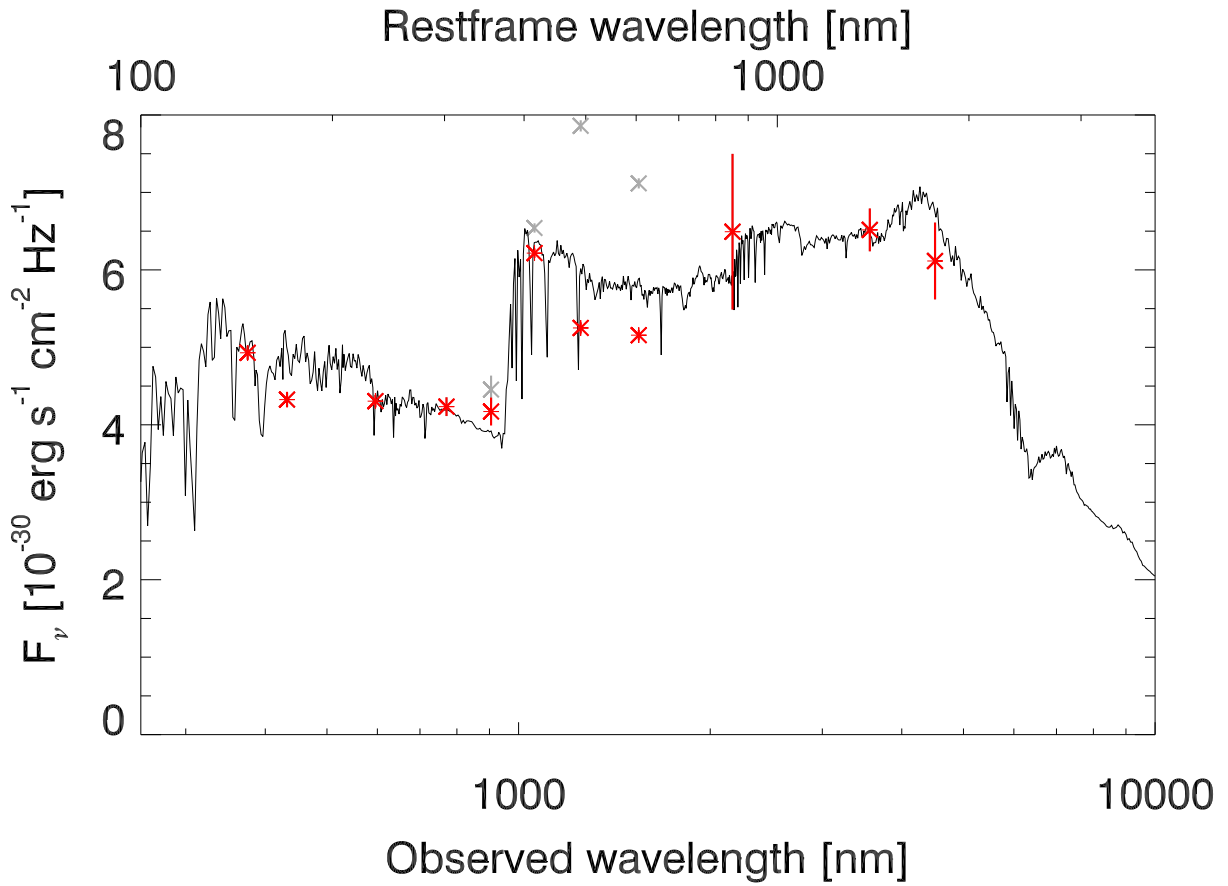


Fig. 2.— The SED of the SN Primo host derived from broad-band photometry. In red (gray) are the photometric points after (before) the subtraction of the emission-line flux. Overplotted is the best-fitting model SED from FAST.

2.3. Photometric Data

To construct the SED for the host of SN Primo, we use photometry from the F160W filter (H-band) selected TFIT catalogue. The photometry in each band is carried out using the TFIT algorithm (Laidler et al. 2007). This method performs point-spread function (PSF) matched photometry uniformly across different instruments and filters, despite their large variations in PSFs and pixel scales. The final catalogue has photometry in VLT/VIMOS (U-band), *HST*/ACS (F435W, F606W, F775W, and F850LP), *HST*/WFC3 (F105W, F125W, and F160W), VLT/ISAAC (K_s), and two *Spitzer*/IRAC channels (3.6 μm and 4.5 μm). The SN search uses the *HST*/WFC3 bands. To get SN free photometry in these bands a set of pre-explosion images from another *HST*/WFC3 survey (GO-11563, PI:Illingworth, see e.g. Oesch et al. 2010) was used. The photometry is listed in Table 1. The *HST* (WFC3) observations are performed as a part of CANDELS project and are further described in Grogin et al. (2011) and Koekemoer et al. (2011). More details on the rest of the filters and observations are given in Dahlen et al. (2010).

3. ANALYSIS

3.1. Broad-Band SED Fitting

The broad-band SED of the host of SN Primo (Table 1) covers rest frame UV to near-IR (200 – 2000 nm). We use the SED fitting code FAST (Kriek et al. 2009) to derive properties such as stellar mass, M_* , and stellar age, t_* . The photometric data is corrected for the strong emission lines detected in the spectrum by subtracting the line flux from the corresponding filters. The strong emission lines are not modeled by the stellar population synthesis models of Bruzual & Charlot (2003) used by FAST. For each filter that has strong emission lines the flux is corrected as

$$F_\nu^{(\text{corr})} = F_\nu - \frac{F_{\text{line}}}{\Delta\nu}, \quad (1)$$

where F_ν is the flux density in the broad-band filter, F_{line} is the flux in the emission line, and $\Delta\nu = \int T(\nu)d\nu \cdot T(\nu_{\text{line}})^{-1}$ is the integral of the filter curve, corrected for the transmission

³As measured by the Paranal on-site seeing monitor

⁴See, <http://www.eso.org/sci/software/pipelines/>

⁵See, <http://www.eso.org/sci/observing/tools/standards/spectra/gd71.html>

⁶<http://www.eso.org/sci/facilities/paranal/instruments/xshooter/doc/>

of the filter at the location of the emission line. We use the same transmission function that is used in FAST for each filter.

The emission-line-subtracted SED is corrected for Galactic extinction (Schlegel et al. 1998, $E(B-V) = 0.008^7$) using a Galactic extinction-law (Cardelli et al. 1989) and $R_V = 3.1$. We use FAST to fit the corrected SED assuming a Chabrier (2003) initial mass function (IMF) and three different star-formation histories (SFH, see Table 2 and Figure 2). The masses, ages and star-formation rates (SFR) derived in Table 2 assuming different SFH agree within the 1σ uncertainties.

We also run the SED fitting without any correction to the broad-band SED, but excluding the J and H band to get a second measure of the physical parameters. This second measure quantifies the systematic shift that the correction procedure can put on the physical parameters. We check that the best fitting parameters of this second fit is within the 1σ error bars. For reference the shift in $\log(M_*)$ is 0.07 higher for the second fit, compared to the upper error bar of 0.13 on our main SED fit.

3.2. Resampling of the X-shooter Spectrum

We correct the spectrum for Galactic extinction in the same manner as the broad-band photometry. To obtain a robust estimate of the uncertainties in the spectral quantities such as the metallicity or line ratios, we re-sample the X-shooter spectrum 10 000 times. For each wavelength bin we resample the flux using the error spectrum (assuming gaussian error). In each iteration the spectral lines are fitted with a gaussian line profile and the centroid, the Full Width at Half Maximum (FWHM), and the total flux is calculated (see Table 3 and Figure 3). The redshift is determined from $H\alpha$, [O II] $\lambda 3729$, [O III] $\lambda\lambda 4959, 5007$ in each iteration. All reported values that are derived from the spectrum are the median values and 68% error bars of the 10 000 samplings. The heliocentric velocity correction is 6.54 km s^{-1} , calculated using the IRAF task `rvcorrect`.

Special care is taken when fitting [O II] $\lambda\lambda 3726, 3729$ and $H\beta$ in each resampling: The blue component of the [O II] doublet, [O II] $\lambda 3726$, is located on top of a sky line. After masking out the sky line it is impossible to fit the peak of [O II] $\lambda 3726$. We therefore fit a double-gaussian line-profile to [O II] $\lambda\lambda 3726, 3729$. We fix the peak of the blue components, λ_{blue} , to the peak of the red component, λ_{red} , by requiring $\lambda_{\text{blue}}/\lambda_{\text{red}} = 372.6032\text{nm}/372.8815\text{nm}$.

⁷Quoted from the NASA/IPAC Extragalactic Database (NED) website: <http://ned.ipac.caltech.edu/>

The flux ratio of the two components is left as a free parameter.

H β is also located on top of a sky line with the wings visible. We remove the sky line in the same manner as for [O II] λ 3726 and fix the wavelength, λ_0 , and FWHM of the fit. λ_0 is fixed to $\lambda_{H\beta}(1+z)$, where $\lambda_{H\beta} = 486.1325\text{nm}$. The FWHM is fixed to the measured FWHM of H α in velocity units. The instrumental broadening of spectral lines is constant if measured in velocity units and therefore affects H α and H β equally. The derived flux may be biased if a gaussian line profile is not a correct description of the line. Due to the uncertainties in the H β detection we will not use the derived flux, other than for constraining the Balmer decrement. For all other purposes we set the flux of H β equal to the flux of H α divided by 2.86 (see discussion in Section 3.3).

We do not detect [N II] λ 6583 in the spectrum. To derive an upper limit of the flux, we measure the standard deviation of the flux density at the location of the line, $\lambda_{\text{NII}}(1+z) \pm 2\Delta\lambda$, where $\lambda_{\text{NII}} = 658.346\text{nm}$ and $\Delta\lambda = \lambda/R$ is the size of one resolution element. Table 3 lists the 5σ upper limit of the non-detection.

3.3. Host Extinction

We correct the X-shooter spectrum for Galactic extinction in the same manner as for the broad-band SED. We test if the A_V from SED fitting is consistent with the spectrum. To gauge the intrinsic extinction from the spectrum we measure the Balmer decrement, H α /H β . By comparing the measured Balmer decrement, B , with the expected $B_0 = 2.86$ given in Osterbrock & Ferland (2006) (case B recombination, $T_e = 10^4$ K), we calculate the extinction as

$$A_V = -2.5 \log \left(\frac{B}{B_0} \right) \frac{k(V)}{k(H\alpha) - k(H\beta)}, \quad (2)$$

where $k(\lambda) = A_\lambda/E(B-V)$: $k(V) \equiv R_V = 3.1$, $k(H\alpha) = 2.468$, and $k(H\beta) = 3.631$ (Calzetti 2001). We assume $R_V = 3.1$ because the SED and the spectrum probe the luminosity weighted average R_V of the host of SN Primo and not just the SN sight line, where a lower R_V (down to ~ 1.7) can be measured (Phillips 2011).

The value $A_V = 0.6^{+1.1}_{-0.7}$ derived from the Balmer decrement is consistent with the value derived from the SED fitting. The large uncertainty in A_V is due to the difficulty in estimating the H β flux (see Section 3.2). For reference, the extinction derived from the SN light curve is $A_V = 0.14 \pm 0.14$ (Rodney et al. 2012), but it does not have to be linked to the (luminosity weighted) average of the galaxy as a whole.

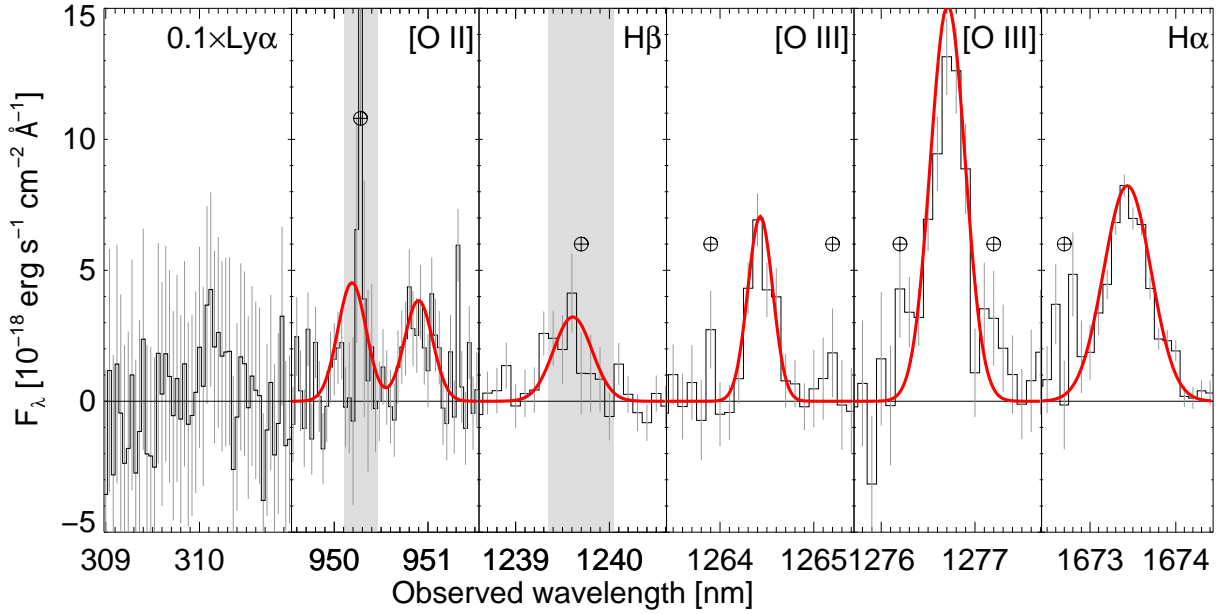


Fig. 3.— The detected emission lines in the X-shooter spectrum of the host of SN Primo. The spectrum is flux-calibrated and corrected for Galactic extinction. The solid (red) line shows the best fitting gaussian line profiles. The $[\text{O II}] \lambda\lambda 3726, 3729$ line is fitted with a double gaussian line profile. The gray bands mark regions excluded due to sky lines. In the $\text{H}\beta$ fit the line center was fixed to $\lambda_{\text{H}\beta}(1+z)$, where $\lambda_{\text{H}\beta} = 486.1325$ nm and z is the redshift. $\text{Ly}\alpha$ is detected, but located close to the Earth’s atmospheric UV cutoff.

3.4. Metallicity

Given that we do not detect [N II] or [S II] lines in our spectrum we will use the line ratio,

$$R_{23} = \log \left(\frac{[\text{O II}]_{\lambda\lambda 3726,3729} + [\text{O III}]_{\lambda\lambda 4959,5007}}{H\beta} \right), \quad (3)$$

to determine the metallicity. We take the average of the two R_{23} calibrations (McGaugh 1991; Kobulnicky & Kewley 2004) as used in Kewley & Ellison (2008) whose procedure we follow.

The R_{23} diagnostic has the problem of being double valued, meaning that from a measured R_{23} value two metallicities can be inferred (see Figure 4). We therefore need an independent measure to break this degeneracy. The upper limit on [N II] $\lambda 6586$ gives an upper limit on

$$\log \left(\frac{[\text{N II}]_{\lambda 6586}}{[\text{O II}]_{\lambda\lambda 3726,3729}} \right) < -1.0. \quad (4)$$

This constrains the metallicity to the low metallicity branch of R_{23} (see Kewley & Dopita 2002, their Figure 3). The low metallicity branch of R_{23} changes with ionization parameter, q . To break the q -degeneracy, we need the line ratio

$$O_{32} = \log \left(\frac{[\text{O III}]_{\lambda 5007}}{[\text{O II}]_{\lambda\lambda 3726,3729}} \right), \quad (5)$$

see Figure 4. The procedure of Kobulnicky & Kewley (2004) is to iterate back and forth between the two plots of Figure 4 until the estimates of metallicity and q converge. In Kobulnicky & Kewley (2004) convergence is achieved after three iterations. We use 10 iterations in our implementation as this makes the convergence independent of the choice of initial guess. The metallicities derived from the two techniques are within the 0.1 dex of each other, which is the expected scatter of the two technics (Kewley & Dopita 2002; Kewley & Ellison 2008). The metallicity of the SN Primo host is $12 + \log\left(\frac{O}{H}\right) = 8.12_{-0.10}^{+0.09}$ or $Z = 0.27 \pm 0.06 Z_{\odot}$, assuming a solar abundance of $12 + \log\left(\frac{O}{H}\right) = 8.69$ (Asplund et al. 2009).

3.5. Star formation

We check whether the emission lines of the host of SN Primo are powered by star formation or AGN activity by plotting $\log([\text{N II}] \lambda 6586/H\alpha)$ versus $\log([\text{O III}] \lambda 5007/H\beta)$ in a BPT diagnostics diagram (Baldwin, Phillips, & Terlevich 1981). The host of SN Primo is located in the star-forming region of Figure 5. We therefore conclude that the $H\alpha$ flux is powered by star formation. We derive the SFR from the $H\alpha$ luminosity. We report the SFR for different

IMFs for comparison (Kennicutt 1998; Brinchmann et al. 2004; Mannucci et al. 2010). Using the stellar mass from SED fitting we calculate the specific SFR, $\text{sSFR} = \text{SFR}/M_*$ from the spectrum and obtain a value of $\sim 10^{-8} \text{ yr}^{-1}$, independent of the IMF and SFH, making the host of SN Primo a starburst galaxy. Our definition of a starburst is based on the sSFR (see, e.g. Sullivan et al. 2006, for a review), see Section 4 for discussion on other definitions.

3.6. Lyman- α

We detect Ly α emission at 2.8σ in the spectrum (see Figure 6). This is possibly the lowest redshift ground-based detection of a cosmological Ly α emitter. The significance of the detection is independent of the systematic error in conversion factor between counts and cgs units (i.e. the flux calibration) at Ly α (Section 2.2).

Given the low significance of the detection we can only give an order-of-magnitude estimate of the Ly α escape fraction (as defined in Atek et al. 2009; Hayes et al. 2011, among others),

$$f_{esc} = \frac{F_{\text{Ly}\alpha}}{8.7F_{\text{H}\alpha}}. \quad (6)$$

We derive the line flux $F_{\text{Ly}\alpha}$ by co-adding the flux in all pixels from $\lambda = 309.97 - 310.68 \text{ nm}$ (corresponding to $v = 0 - 600 \text{ km s}^{-1}$). The derived flux estimate is corrected for extinction in the host galaxy. The deviation from the expected value of 8.7 (case B recombination, Brocklehurst 1971) will be due to conditions in the interstellar medium (ISM) like the presence of dust, ISM clumpiness or due to geometric effects that will suppress or enhance the amount of Ly α photons that can escape the galaxy. At a redshift of $z = 1.5$ the universe is fully ionized, absorption of Ly α in the intergalactic medium is therefore not important. We will not try to distinguish between these different scenarios. We include a systematic uncertainty of 40% in the derived Ly α escape fraction, due to the uncertainty in the conversion factor between counts and cgs units at the Ly α wavelength.

4. DISCUSSION & CONCLUSIONS

We have performed a photometric and spectroscopic study of the SN Primo host galaxy. We find a young Large Magellanic Cloud (LMC) sized ($\sim 4.5 \text{ kpc}$) galaxy with LMC-like ($\sim \frac{1}{3}Z_{\odot}$) metallicity and low intrinsic extinction. We confirm that the emission lines are generated by star formation and derive a SFR of almost one order of magnitude larger than that of the LMC. The stellar mass derived from SED fitting is one order of magnitude lower

then the LMC. From the Ly α line we estimate a high escape fraction of Ly α photons. All host properties are summarized in Tables 2 and 4.

In Figure 7 we plot the SFR vs. stellar mass for the host of SN Primo in comparison to both a low redshift (Lampeitl et al. 2010, $z < 0.21$) and two high redshift samples from HST (Thomson & Chary 2011, $0.95 < z < 1.8$) and SNLS (Sullivan et al. 2010, $0.2 < z < 1.0$) samples. The host of SN Primo clearly stands out from the low- z sample, due to its high specific star-formation rate. The relation between SFR and stellar mass is expected to evolve with redshift as seen in observations (Daddi et al. 2007; Elbaz et al. 2007). If SN host galaxies are representative of field galaxies the blue points in Figure 7 are expected to shift upwards in the same way as the green dashed lines (signifying $z = 0, 1, \text{ and } 2$). It is hard to see that trend from the SNLS and HST samples due to the scatter (HST) and degeneracies (SNLS) in the data. The degeneracies (at constant sSFR) in the SNLS data is due to shortcomings in the SED fitting in Sullivan et al. (2010).

Its derived metallicity is not unusually low for galaxies in general, but the metallicity is very low for SN Ia host galaxies (Gallagher et al. 2005; Prieto et al. 2008). We plot the metallicity-luminosity relation for the sample of Prieto et al. (2008, $z < 0.04$). The host of SN Primo has a lower metallicity than any of the low- z galaxies (see Figure 8). The host of SN Primo also falls below the mass-metallicity relation (Tremonti et al. 2004). We check why this could be the case by comparing the host of SN Primo to the Fundamental Metallicity Relation (FMR) of star-forming galaxies (Lara-López et al. 2010; Mannucci et al. 2010) which relates metallicity, stellar mass, and SFR. Mannucci et al. (2011) updated the low-mass slope of the FMR relation using GRB host galaxies. The metallicity predicted by the FMR relation is within the error bars of the measured metallicity. The residual between SN Primo and the FMR relation is $\Delta[12 + \log(\frac{O}{H})] = 0.07 \pm 0.15$. The host of SN Primo is therefore consistent with the FMR relation defined in Mannucci et al. (2011). The FMR relation is consistent with a simple model (Dayal et al. 2012) where the balance of gas infall, outflow, and star formation brings out the relation between SFR, metallicity and stellar mass seen in the FMR relation.

The stellar age of $\sim 10^{8.6}$ years (Table 2) could give an upper limit on the delay time of SN Primo, assuming there is no underlying old stellar population. This would put SN Primo in the prompt progenitor distribution (see Sullivan et al. 2006, for a review). There are however caveats to the values derived from our SED fitting. It is assumed that there is no underlying old stellar population, which can not be ruled out. This is also seen in Table 2 where ages up to $\sim 10^9$ are still consistent within 1σ .

In this paper we have used a redshift independent definition of a starburst based on the value of the sSFR ($\log(sSFR) > -9.5$, Sullivan et al. 2006). Alternatively a starburst can

be defined based on the SFR and M_* of galaxies at the same redshift — the so called main-sequence (MS) of galaxies (indicated in Figure 7a). The evolution of the MS with redshift, however, is not fully settled (see Daddi et al. 2007; Wuyts et al. 2011; Whitaker et al. 2012, among other). As indicated in Figure 7a the MS fits at $z = 1$ and $z = 2$ would have to be extrapolated down to the mass of the host of SN Primo.

Gallagher et al. (2005) showed that the light-curve shape correlates with the Hubble type of the host galaxy and Meyers et al. (2012) showed that both light-curve shape and SN peak color are different between early-type and late-type galaxies. Sullivan et al. (2011) showed by splitting up the SNLS3 sample of SNe Ia into a high and low sSFR sample, that the host galaxy has an influence on the mean SN peak brightness and the correction of light-curve shape and color correction. Galaxy evolution models find that sSFR increases with redshift out to at least $z = 2$. Using the mass of the host of SN Primo the “host term” of Kelly et al. (2010) is 0.3 mag (super-luminous SN). These dependencies highlight that the bulk of the training sample of SNe Ia lies below $z < 1$ where the host galaxies are older and in general have a smaller sSFR. As a consequence, this could introduce a potential bias in the distances derived to the high sSFR host galaxies, when not explicitly including the host correction. As the sample of high redshift and high sSFR SNe grows the size of this effect can be investigated further.

We thank Robert Kirshner, Mark Dickinson, Peter M. Garnavich, Brian Hayden, Giorgos Leloudas for comments and discussions. We thank the anonymous referee for valuable comments that helped improve this manuscript. We thank Martin Sparre for providing his X-shooter meta-pipeline, which has simplified the reduction of the X-shooter spectra significantly. This work is based on observations taken by the CANDELS Multi-Cycle Treasury Program with the NASA/ESA HST, which is operated by the Association of Universities for Research in Astronomy, Inc., under NASA contract NAS5-26555. The Dark Cosmology Centre is funded by the Danish National Research Foundation. This research has made use of the NASA/IPAC Extragalactic Database (NED) which is operated by the Jet Propulsion Laboratory, California Institute of Technology, under contract with the National Aeronautics and Space Administration.

Facilities: VLT:Kueyen (X-shooter), HST (ACS, WCF3), VLT:Melipal (ISAAC, VIMOS), Spitzer (IRAC)

REFERENCES

Asplund, M., Grevesse, N., Sauval, A. J., & Scott, P. 2009, ARA&A, 47, 481

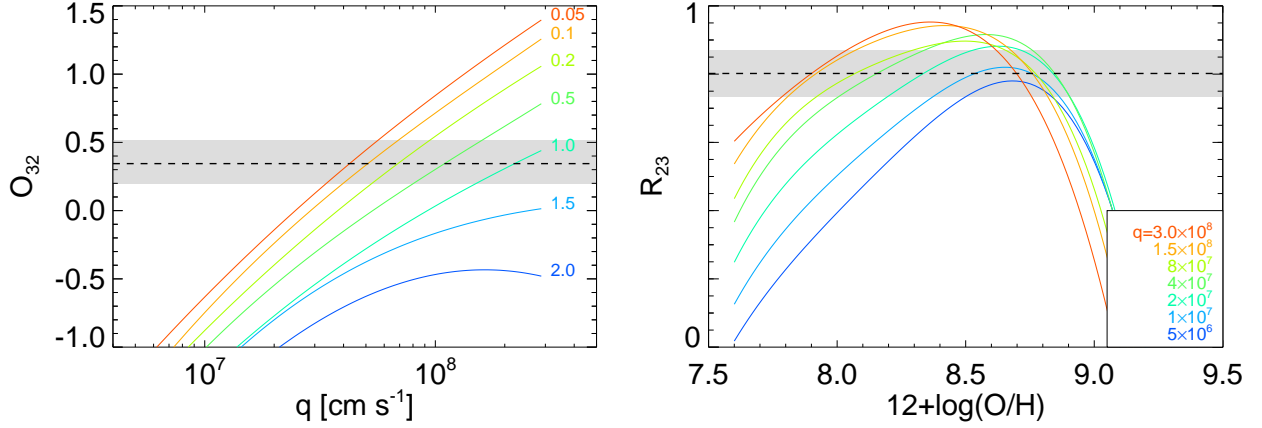


Fig. 4.— The O_{32} and R_{23} line ratios of the host of SN Primo together with the photoionization models of Kewley & Dopita (2002). The dashed lines and gray bands show the line ratios and 1σ error bars derived from the spectrum. Left: O_{32} (Equation 5) versus the ionization parameter q . From top down the metallicities are $Z = 0.05, 0.1, 0.2, 0.5, 1.0, 1.5$, and $2.0 Z_{\odot}$. Right: R_{23} (Equation 3) versus the metallicity. From the top down $q = 30, 15, 8, 4, 2, 1, 0.5 \times 10^7 \text{ cm s}^{-1}$.

Table 1. Photometry of the host of SN Primo

Filter	Instrument	λ_{eff} (nm)	Magnitude ^a (AB mag)	Corrected ^b (AB mag)
U-band	VLT/VIMOS	375.3	24.69 ± 0.02	...
F435W (B)	<i>HST</i> /ACS	432.8	24.84 ± 0.02	...
F606W (V)	<i>HST</i> /ACS	595.8	24.84 ± 0.02	...
F775W (i)	<i>HST</i> /ACS	770.6	24.86 ± 0.03	...
F850LP (z)	<i>HST</i> /ACS	905.3	24.80 ± 0.04	24.88 ± 0.04
F105W (Y)	<i>HST</i> /WFC3	1059	24.50 ± 0.01	24.56 ± 0.01
F125W (J)	<i>HST</i> /WFC3	1252	24.27 ± 0.01	24.71 ± 0.01
F160W (H)	<i>HST</i> /WFC3	1544	24.36 ± 0.01	24.71 ± 0.01
K _s -band	VLT/ISAAC	2168	24.47 ± 0.17	...
Channel 1	<i>Spitzer</i> /IRAC	3563	24.43 ± 0.05	...
Channel 2	<i>Spitzer</i> /IRAC	4511	24.49 ± 0.09	...

^aThe magnitudes before subtraction of the emission-line fluxes.

^bThe magnitudes after subtraction of the emission-line fluxes.

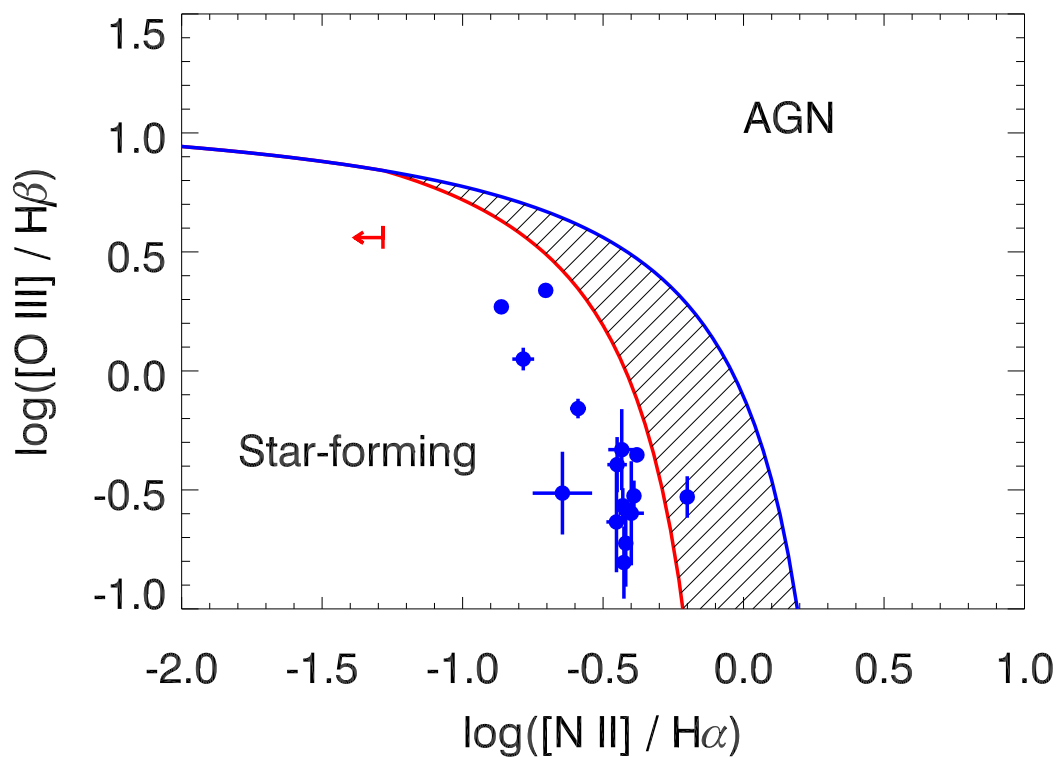


Fig. 5.— BPT diagnostic diagram (Baldwin, Phillips, & Terlevich 1981). The x-axis denotes the ratio $\log([\text{N II}] \lambda 6586 / \text{H}\alpha)$ and the y-axis the ratio $\log([\text{O III}] \lambda 5007 / \text{H}\beta)$. The data point marks the host galaxy of SN Primo, with the arrow denoting the upper-limit of the ratio derived from the non-detection of $[\text{N II}] \lambda 6586$. The vertical bar denotes the 1σ error bar of the ratio. For illustrative purposes we overplot the 15 emission-line hosts from the Lampeitl et al. (2010) sample of SN Ia host galaxies with SDSS spectra.

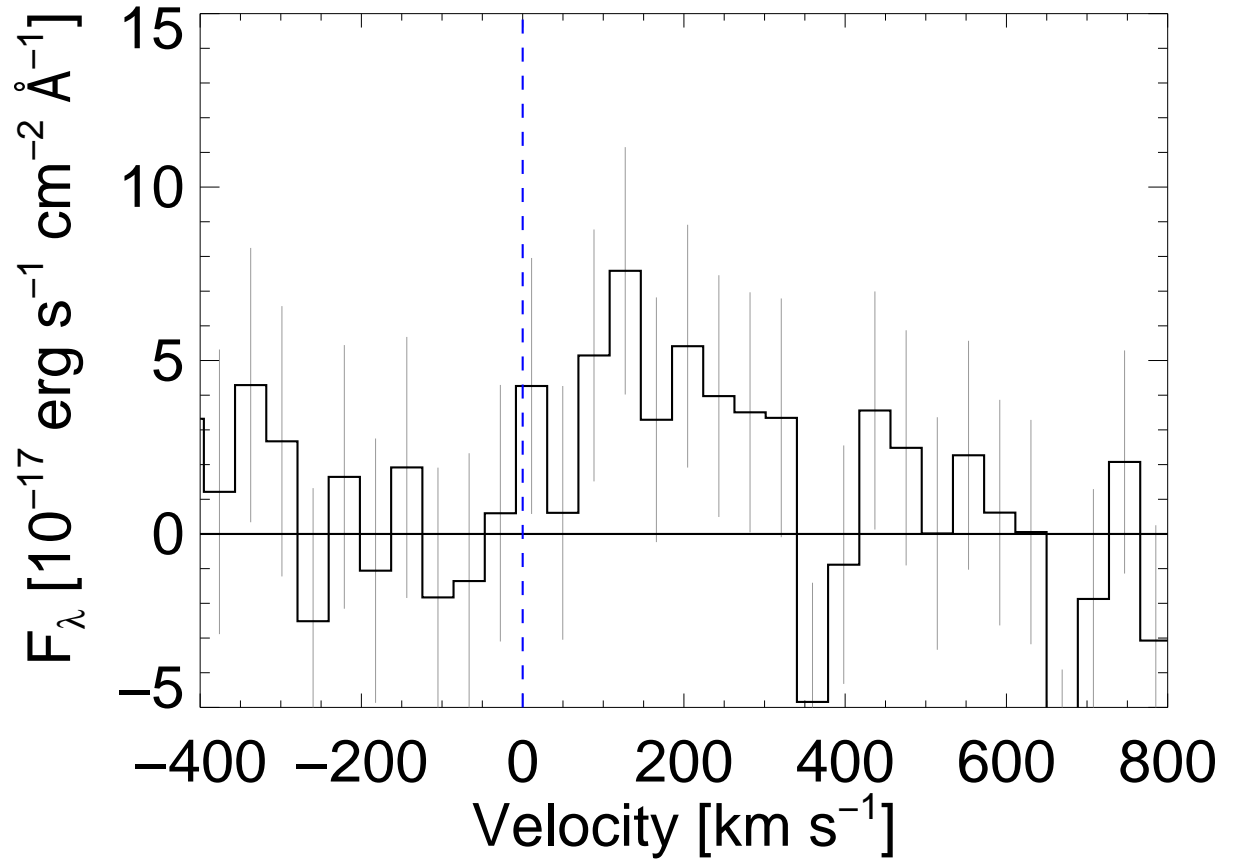


Fig. 6.— The Lyman- α line in the SN Primo host spectrum. The systemic velocity is determined from H α , [O III] $\lambda\lambda$ 4959, 5007, and [O II] λ 3729.

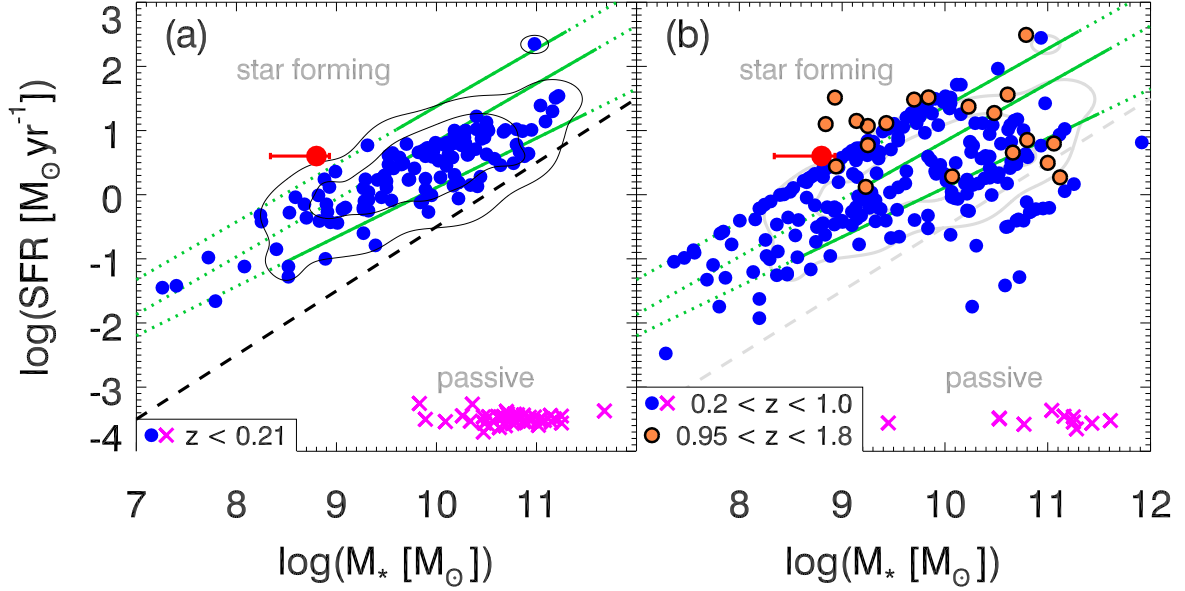


Fig. 7.— The SFR-mass relation for SN Ia host galaxies. The (red) asterisk denotes the host of SN Primo with error bars. Filled (blue) circles mark star-forming hosts in each sample. The (magenta) crosses marks the passive hosts in each sample. The solid and dotted (green) lines show the correlation between SFR and stellar mass for $z \sim 0$ (bottom), $z = 1$ (middle), and $z = 2$ (top) from Daddi et al. (2007, $z = 2$) and Elbaz et al. (2007, $z \sim 0$ and $z = 1$). The solid section of each line marks the range of validity of the relations. (a) The low redshift sample ($z < 0.21$) from SDSS (Lampeitl et al. 2010). The dashed line marks the cut, $\log(sSFR) = -10.6$, between star forming and passive galaxies. The contours mark the region enclosing 68% and 95% of the star-forming sample. (b) The high redshift samples from HST (Thomson & Chary 2011, $0.95 < z < 1.8$, open (orange) circles) and SNLS (Sullivan et al. 2010, $0.2 < z < 1.0$, filled (blue) circles / (magenta) crosses). The apparent upper diagonal ridge-line for the Sullivan et al. (2010) data is due to shortcomings in their SED fitting.

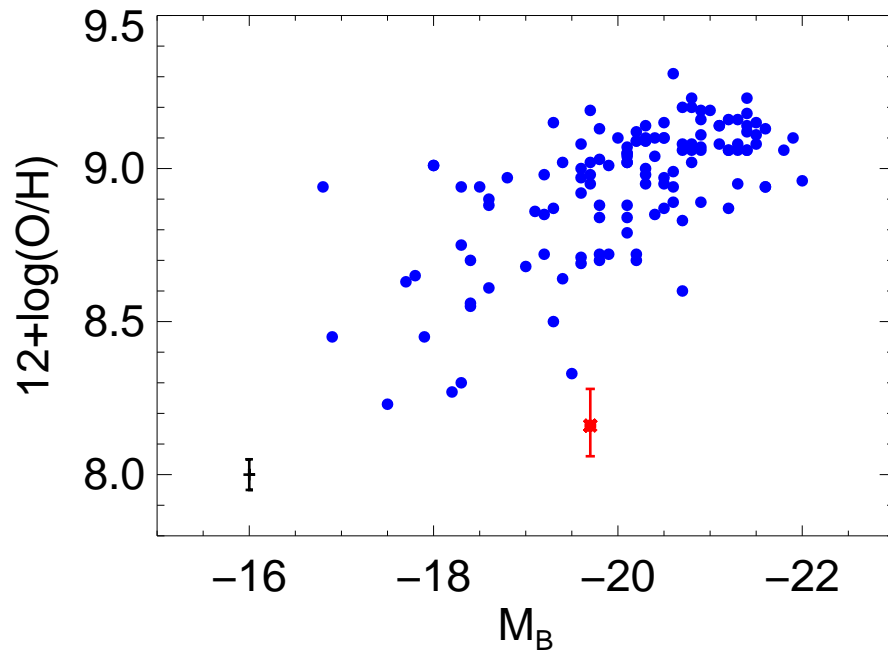


Fig. 8.— Metallicity–luminosity relation for SN Ia host galaxies. The (red) asterisk denotes the host of SN Primo with error bars. The (blue) filled circles denotes the sample of Prieto et al. (2008, $z < 0.04$, median error bar plotter to the lower left).

Table 2. Summary of SED fitting using FAST.

Parameter ^a	Exponential ^b	Delayed ^c	Truncated ^d
$\log(t_*[\text{yr}])$	$8.50^{+0.28}_{-1.41}$	$8.60^{+0.51}_{-1.25}$	$8.65^{+0.13}_{-1.20}$
$\log(\tau[\text{yr}])$	$8.80^{+2.20}_{-2.30}$	$8.30^{+2.70}_{-1.62}$	$9.40^{+1.60}_{-1.96}$
Z	$0.020^{+0.023}_{-0.016}$	$0.020^{+0.021}_{-0.016}$	$0.020^{+0.015}_{-0.016}$
A_V	$0.00^{+0.71}_{-0.00}$	$0.00^{+0.71}_{-0.00}$	$0.00^{+0.70}_{-0.00}$
$\log(M_*[\text{M}_\odot])$	$8.80^{+0.13}_{-0.46}$	$8.81^{+0.16}_{-0.34}$	$8.84^{+0.07}_{-0.39}$
$\log(SFR[\text{M}_\odot\text{yr}^{-1}])$	$0.33^{+0.77}_{-0.87}$	$0.32^{+0.84}_{-0.49}$	$0.35^{+0.73}_{-0.99.35}$
$\log(sSFR[\text{yr}^{-1}])$	$-8.47^{+1.07}_{-0.61}$	$-8.49^{+1.15}_{-0.27}$	$-8.50^{+1.06}_{-0.90.50}$
$\log(t_*/\tau)$	$-0.30^{+1.05}_{-3.25}$	$0.30^{+0.50}_{-3.60}$	$-0.75^{+0.80}_{-2.75}$
$\tilde{\chi}^2$	19.9	19.8	19.8

^aWe have assumed a Chabrier IMF

^bExponential star-formation history: $SFR(t) \propto \exp(-t/\tau)$, $\tau > 0$

^cDelayed star-formation history: $SFR(t) \propto t \cdot \exp(-t/\tau)$

^dTruncated star-formation history: $SFR(t) = \text{constant}$; for $t \in [t_*, t_* + \tau]$, else 0

Table 3. Emission lines detected in the spectrum of the host of SN Primo.

Line	Wavelength [nm]	Observed	FWHM [nm]	[km s ⁻¹]	Flux ^a [10 ⁻¹⁷ erg s ⁻¹ cm ⁻²]
H α λ 6563	1673.43 ^{+0.01} _{-0.02}	0.65 ^{+0.05} _{-0.04}	117 ⁺⁸ ₋₇	5.1 ^{+0.3} _{-0.3}	
[O III] λ 5007	1276.71 ^{+0.02} _{-0.02}	0.44 ^{+0.07} _{-0.05}	103 ⁺¹⁶ ₋₁₁	6.0 ^{+0.6} _{-0.5}	
[O III] λ 4959	1264.43 ^{+0.04} _{-0.03}	0.31 ^{+0.07} _{-0.08}	75 ⁺¹⁶ ₋₁₇	2.1 ^{+0.4} _{-0.4}	
H β λ 4861 ^b	-	-	-	1.4 ^{+0.4} _{-0.5}	
[O II] $\lambda\lambda$ 3726,3729 ^c	950.90 ^{+0.08} _{-0.05}	0.35 ^{+0.27} _{-0.07}	112 ⁺⁸⁶ ₋₂₁	2.6 ^{+1.0} _{-0.8}	
[N II] λ 6586 ^d	-	-	-	< 0.3	
Ly α λ 1216 ^e	-	-	-	11.2 ^{+4.0} _{-3.9}	

^aFit of the observed flux corrected for Galactic extinction ($E(B - V) = 0.008$).

^bIn each resampling the following fit was performed: The central-wavelength of the line was fixed to $\lambda_{H\beta}(1 + z)$, where $\lambda_{H\beta} = 486.1325\text{nm}$ and z is the redshift. $\text{FWHM}(H\beta)$ was fixed to $\text{FWHM}(H\alpha)$ in velocity units. Only the peak intensity was allowed to vary.

^cThe wavelength is that of [O II] λ 3729 (the red component) only, the flux is the sum of both components.

^d 5σ upper limit of the non-detection.

^eThe Ly α flux is the co-added flux from $v = 0 - 600 \text{ km s}^{-1}$. The error bars only cover the statistical errors. The systematic error is $\sim 40\%$.

Table 4. Spectroscopic summary.

Parameter	Value	Assumed IMF
Redshift (heliocentric)	$z = 1.54992^{+0.00008}_{-0.00004}$	
Metallicity	$12 + \log(\frac{O}{H}) = 8.12^{+0.09}_{-0.10}$ $Z = 0.27^{+0.06}_{-0.06} Z_{\odot}$ ^a	
Extinction	$A_V = 0.6^{+1.1}_{-0.7}$ mag	
Ly α escape fraction	$f_{esc} = 0.25 \pm 0.09$ (± 0.10) ^b	
Star-formation rate:		
	$SFR = 6.4 \pm 0.3 M_{\odot} \text{ yr}^{-1}$	Salpeter
	$SFR = 4.3 \pm 0.2 M_{\odot} \text{ yr}^{-1}$	Kroupa
	$SFR = 3.8 \pm 0.2 M_{\odot} \text{ yr}^{-1}$	Chabrier
Specific star-formation rate:		
	$\log(sSFR[\text{yr}^{-1}]) = -7.8 \pm 0.2$	Salpeter
	$\log(sSFR[\text{yr}^{-1}]) = -8.0 \pm 0.2$	Kroupa
	$\log(sSFR[\text{yr}^{-1}]) = -8.1 \pm 0.2$	Chabrier

^aAssuming a solar oxygen abundance of 8.69 (Asplund et al. 2009)

^bThe value in parenthesis covers the systematic uncertainty on the flux of Ly α of 40%.

- Atek, H., Kunth, D., Schaerer, D., Hayes, M., Deharveng, J. M., Östlin, G., & Mas-Hesse, J. M. 2009, *A&A*, 506, L1
- Baldwin, J. A., Phillips, M. M., & Terlevich, R. 1981, *PASP*, 93, 5
- Brinchmann, J., Charlot, S., White, S. D. M., Tremonti, C., Kauffmann, G., Heckman, T., & Brinkmann, J. 2004, *MNRAS*, 351, 1151
- Brocklehurst, M. 1971, *MNRAS*, 153, 471
- Bruzual, G., & Charlot, S. 2003, *MNRAS*, 344, 1000
- Calzetti, D. 2001, *PASP*, 113, 1449
- Cardelli, J. A., Clayton, G. C., & Mathis, J. S. 1989, *ApJ*, 345, 245
- Chabrier, G. 2003, *PASP*, 115, 763
- Conley, A., et al. 2011, *ApJS*, 192, 1
- Daddi, E., et al. 2007, *ApJ*, 670, 156
- Dahlen, T., et al. 2010, *ApJ*, 724, 425
- Dayal, P., Ferrara, A., & Dunlop, J. S. 2012, *ArXiv e-prints*, arXiv:1202.4770
- D’Odorico, S., et al. 2006, in *Society of Photo-Optical Instrumentation Engineers (SPIE) Conference Series*, Vol. 6269
- Elbaz, D., et al. 2007, *A&A*, 468, 33
- Gallagher, J. S., Garnavich, P. M., Berlind, P., Challis, P., Jha, S., & Kirshner, R. P. 2005, *ApJ*, 634, 210
- Grogin, N. A., et al. 2011, *ApJS*, 197, 35
- Hamuy, M., Trager, S. C., Pinto, P. A., Phillips, M. M., Schommer, R. A., Ivanov, V., & Suntzeff, N. B. 2000, *AJ*, 120, 1479
- Hayes, M., Schaerer, D., Östlin, G., Mas-Hesse, J. M., Atek, H., & Kunth, D. 2011, *ApJ*, 730, 8
- Hillebrandt, W., & Niemeyer, J. C. 2000, *ARA&A*, 38, 191
- Kelly, P. L., Hicken, M., Burke, D. L., Mandel, K. S., & Kirshner, R. P. 2010, *ApJ*, 715, 743

- Kennicutt, Jr., R. C. 1998, *ARA&A*, 36, 189
- Kewley, L. J., & Dopita, M. A. 2002, *ApJS*, 142, 35
- Kewley, L. J., & Ellison, S. L. 2008, *ApJ*, 681, 1183
- Kirshner, R. P. 2010, *Foundations of supernova cosmology*, ed. P. Ruiz-Lapuente, 151
- Kobulnicky, H. A., & Kewley, L. J. 2004, *ApJ*, 617, 240
- Koekemoer, A. M., et al. 2011, *ApJS*, 197, 36
- Komatsu, E., et al. 2011, *ApJS*, 192, 18
- Kriek, M., van Dokkum, P. G., Labbé, I., Franx, M., Illingworth, G. D., Marchesini, D., & Quadri, R. F. 2009, *ApJ*, 700, 221
- Laidler, V. G., et al. 2007, *PASP*, 119, 1325
- Lampeitl, H., et al. 2010, *ApJ*, 722, 566
- Lara-López, M. A., et al. 2010, *A&A*, 521, L53+
- Mannucci, F., Cresci, G., Maiolino, R., Marconi, A., & Gnerucci, A. 2010, *MNRAS*, 408, 2115
- Mannucci, F., Salvaterra, R., & Campisi, M. A. 2011, *MNRAS*, 414, 1263
- March, M. C., Trotta, R., Berkes, P., Starkman, G. D., & Vaudrevange, P. M. 2011, *MNRAS*, 418, 2308
- McGaugh, S. S. 1991, *ApJ*, 380, 140
- Meyers, J., et al. 2012, *ApJ*, 750, 1
- Oesch, P. A., et al. 2010, *ApJ*, 709, L16
- Osterbrock, D. E., & Ferland, G. J. 2006, *Astrophysics of gaseous nebulae and active galactic nuclei* (University Science Books)
- Perlmutter, S., et al. 1999, *ApJ*, 517, 565
- Phillips, M. M. 1993, *ApJ*, 413, L105
- . 2011, *ArXiv e-prints*, arXiv:1111.4463

- Phillips, M. M., Lira, P., Suntzeff, N. B., Schommer, R. A., Hamuy, M., & Maza, J. 1999, *AJ*, 118, 1766
- Prieto, J. L., Stanek, K. Z., & Beacom, J. F. 2008, *ApJ*, 673, 999
- Riess, A. G., & Livio, M. 2006, *ApJ*, 648, 884
- Riess, A. G., Press, W. H., & Kirshner, R. P. 1996, *ApJ*, 473, 88
- Riess, A. G., et al. 1998, *AJ*, 116, 1009
- Rodney, S. A., et al. 2012, *ApJ*, 746, 5
- Schlegel, D. J., Finkbeiner, D. P., & Davis, M. 1998, *ApJ*, 500, 525
- Sullivan, M., et al. 2006, *ApJ*, 648, 868
- . 2010, *MNRAS*, 406, 782
- . 2011, *ApJ*, 737, 102
- Suzuki, N., et al. 2012, *ApJ*, 746, 85
- Thomson, M. G., & Chary, R. R. 2011, *ApJ*, 731, 72
- Tremonti, C. A., et al. 2004, *ApJ*, 613, 898
- Vernet, J., et al. 2011, *A&A*, 536, A105
- Wang, B., & Han, Z. 2012, *New A Rev.*, 56, 122
- Whitaker, K. E., van Dokkum, P. G., Brammer, G., & Franx, M. 2012, *ApJ*, 754, L29
- Wilson, O. C. 1939, *ApJ*, 90, 634
- Wuyts, S., et al. 2011, *ApJ*, 742, 96
- Zwicky, F. 1938, *Physical Review*, 53, 1019